

A Confocal Raman Imaging Study of an Optically Transparent Boron-Doped Diamond Electrode

Michel Mermoux,^{*,†} Bernadette Marcus,[†] Greg. M. Swain,[‡] and James E. Butler[§]

Laboratoire d'Electrochimie et de Physicochimie des Matériaux et des Interfaces, UMR 5631 INPG-CNRS, associé à l'UJF, Domaine Universitaire, BP75, 38402 Saint Martin d'Hères cedex, France, Department of Chemistry, Michigan State University, 320 Chemistry Building, East Lansing, MI 48824-1322, and Naval Research Laboratory, Chemistry Division, Code 6174, Washington, DC 20375-5000

Received: January 30, 2002; In Final Form: June 17, 2002

Confocal micro-Raman imaging was used to investigate the structural and, to some extent, the chemical inhomogeneities that exist in a high-quality, free-standing, polished, optically transparent boron-doped chemical-vapor-deposition (CVD) diamond disk. A number of boron-related Raman lines centered at about 610, 925, 1045, 1375, and 1470 cm^{-1} were evidenced and found to vary from one region of the disk to another. These lines have previously been reported in the literature for other boron-doped crystals or films obtained using completely different growth conditions. Even if their origin is still somewhat uncertain, their presence enabled the construction of spatial maps of the boron signal intensity over the surface. It was confirmed that boron is incorporated into CVD diamond with significant inhomogeneities. In most cases, the boron signal intensity tracked the structure of the grains. The high quality of the disk also allowed a detailed analysis of the grain boundaries to be made. However, a unique description of these grain boundaries in terms of their microstructure and chemical composition could not be developed. There is some evidence that nondiamond phases are incorporated into the grain boundaries, but their Raman signature is quite distinct from that usually reported. Another remarkable feature of this disk is that it is nearly photoluminescence-free. Photoluminescence, as excited by the 514.5 or 457.9 nm lines of an argon ion laser, was only detected within some of the nondiamond amorphous carbon-rich grain boundaries. The low photoluminescence background was also a common feature of a heavily boron-doped, polycrystalline film deposited on silicon, another sample that was also examined in this work for comparison. Despite its high quality, the optically transparent disk is far from being stress-free. Localized stress variations were observed. The strained regions are not systematically associated with the incorporation of nondiamond carbon. Grain boundaries and, most probably, planar defects have been identified as the stress sources. However, it remains difficult to explain the large compressive stress observed for some of the crystals.

Introduction

Boron is a well-established p-type dopant that controls the electrical conductivity in diamond. It may be introduced into the material during deposition and a wide range of boron concentrations have been achieved, up to a few percent. However, the amount incorporated depends on the particular growth sector.^{1–5} For the case of polycrystalline diamond films obtained by chemical vapor deposition (CVD) techniques, there are a number of papers describing the spatially inhomogeneous distribution of boron. For example, the dopant concentration in the $\langle 111 \rangle$ growth sector is approximately 1 order of magnitude higher than that in the $\langle 100 \rangle$ sector.^{3,4} It may be also supposed that boron can aggregate in the grain boundaries of polycrystalline films, and in such a case, these dopant atoms will not function electronically in terms of providing charge carriers. Others have suggested a grain-size or grain-boundary dependence on the uptake.^{6,7} In certain potential applications of diamond, uniform electronic properties are required over the

micrometer domain. Therefore, microscopic probes of the local boron-doping level, morphology, and microstructure are needed to fully understand the macroscopic properties of the material.

Boron-doped diamond electrodes possess several properties useful for electrochemistry.^{8,9} In recent years, several groups have made progress in understanding some of the factors that control the electrochemical response of diamond. However, the relationship between the physical, chemical, and electronic properties and the electrochemical response is still not fully elucidated. Microcrystalline diamond thin films have been the most studied form of the material so far. The electrochemical properties appear to be influenced in a complex manner by (i) the dopant concentration, (ii) morphological features such as grain boundaries and extended and point defects, (iii) the nondiamond (amorphous sp^2/sp^3 bonded phases) carbon content at the surface, (iv) the crystallographic orientation, and (v) the surface termination. Moreover, the degree to which these factors influence the electrochemical response is strongly dependent on the electrode reaction mechanism for a particular redox analyte. Thus, an understanding of how the electrochemical properties are influenced by these factors requires the ability to characterize and spatially distinguish these features within the film.

* To whom correspondence should be addressed. E-mail: Michel.Mermoux@lepmi.inpg.fr.

[†] INPG-CNRS.

[‡] Michigan State University.

[§] Naval Research Laboratory.

Raman scattering and photoluminescence (PL) spectroscopy are widely used tools for the characterization of impurities, defects, and structural imperfections in diamond.^{10,11} The development of micro-Raman analysis techniques enables one to investigate the impurities, defects, and structural imperfections in diamond films with micrometer resolution.

We report presently on the use of confocal micro-Raman and photoluminescence imaging spectroscopy to investigate the microstructural inhomogeneities and chemical impurities that exist in two types of synthetic diamond electrodes: a free-standing, boron-doped optically transparent polished diamond disk [sample A] and a boron-doped polycrystalline film deposited on silicon (Si) [sample B]. The electrochemical and optical properties of the diamond disk [sample A] were reported previously.¹² The characteristics of sample A, in particular the large grain size (ca. 50 μm) and low surface roughness (root-mean-square roughness of ca. 7 nm after mechanical polishing), have allowed us to examine the grain and grain boundary regions in significant detail (boron content, strain, impurities, ...).

The long-term goal of our work with optically transparent diamond disks is to develop usable electrodes for spectroelectrochemical measurements in the UV/vis/IR regions of the electromagnetic spectrum. To develop such electrodes, we need to understand how manipulation of the growth conditions affects the macroscopic and microscopic optical properties. Raman and PL imaging spectroscopy can provide microscopic information about the microstructure, boron-doping level, and defect structure of the electrodes.

Experimental Section

Raman and Photoluminescence Measurements. A DILOR XY triple monochromator spectrometer was used for the combined Raman and PL measurements, equipped with a liquid nitrogen cooled multichannel CCD detector. The samples were mounted on a computer-controlled XY table, movable in 100 nm steps. During a Raman (or PL) mapping, the full spectra for each point were recorded and stored in an "image file". Therefore, after mapping, the data contained the complete locally resolved information within the studied spectral window and sample area. The width of the spectral window depends on the excitation wavelength and especially on the acquisition mode of the spectrometer, double subtractive or triple additive modes. Spectral windows of ~ 1000 and 200 cm^{-1} are available for "low-dispersion" (double subtractive mode) and "high-dispersion" (triple additive mode) measurements, respectively. The result is that the probed area of the sample can be visualized for each wavenumber or integrated wavenumber range to produce 2D spectral images. To create the 2D spectral images, the spectra can be processed by one of the following ways: (i) calculating the integral intensity of the signal in a selected spectral range for each studied sample point (this is a very fast on-screen method, which allows an immediate examination of the results) or (ii) using a band fitting procedure (In this case, one or two lines are extracted from the "image file", and each individual spectrum is fitted using a Gaussian, a Lorentzian, or a mixed Gaussian-Lorentzian line shape. The parameters of the line can thus be plotted as a function of the spatial coordinates). This second method has been systematically used to extract the frequency and the width of the diamond Raman line. The accuracy on the frequency values depends both on the signal-to-noise ratio of the measurement (the acquisition time of each individual spectrum should be chosen suitably) and on the stability of the spectrometer during the acquisition. Various measurements on electronic devices have shown that this

accuracy can be better than 0.03 cm^{-1} . However, as we shall see, the Raman line of diamond is very often deformed by stress effects. In such a case, the frequency extracted for every experimental spectrum is rather a measurement of the center of gravity of the line. A final routine was applied for all the images to smooth the pixel-like appearance of the rough data.

For microscopic spectral measurements, an Olympus microscope equipped with $\times 10$ (numerical aperture (na) = 0.25), long working distance $\times 50$ (na = 0.55), and $\times 100$ (na = 0.95) objectives was used. A confocal diaphragm being adjustable in size from 100 to 1000 μm provides the lateral and axial resolution of the measurements. For the $\times 100$ objective, a 200 μm confocal diaphragm value corresponds to a sampling volume of approximate dimensions 0.7 μm in diameter and 2 μm in thickness. When the $\times 10$ objective is used, the probing depth has been estimated to be higher than 50 μm for transparent materials. The $\times 10$ objective was mostly used to get a first rough estimate of the sample bulk characteristics.

Different lines from an Ar^+ laser were used for excitation: 514.5, 488.0, and 457.9 nm. During the experiments, the power of the incident light has been changed from 10 to 100 mW; no differences about the position of diamond Raman peak have been detected, so heating induced by the laser light as the origin of the differences of peak positions could be excluded.

For the PL measurements, the spectra have been only roughly corrected for instrument response. Some of the measurements have been conducted at the liquid nitrogen temperature using a homemade low-temperature cell designed to work under the microscope and the $\times 50$ long working distance objective.

Samples. Two different boron-doped samples were examined. Sample A was a self-supported 380 μm thick disk of 8 mm diameter. This free-standing polycrystalline diamond disk was grown by microwave plasma CVD (2.45 GHz) in a customized reactor at the Naval Research Laboratory (reference lot no. NRL149). Boron doping was achieved using B_2H_6 prediluted in hydrogen. Growth was achieved on refractory metal substrates (Mo, W), which released free-standing plates on cooling from the deposition temperature. The diamond plate was subsequently laser-machined to appropriate sample size. It was then mechanically polished, cleaned by boiling in aqua regia and then in concentrated sulfuric-fuming nitric acid (3:2 vol) with added sodium nitrate, washed in hydrofluoric acid and then deionized water, and rehydrogenated in a hydrogen plasma, first at 800 $^\circ\text{C}$ then cooled in plasma to 300 $^\circ\text{C}$. Its full description, including growth condition, optical, and electrochemical properties is found in ref 12. Examined with an optical microscope, this film exhibited a blue color, especially when it was illuminated in transmission. This blue color was characteristic of boron doping; however, it was not homogeneous over the sample, varying from light to deep blue.

The first Raman spectra recorded for this sample presented unusual weak signals in the 600–1100 cm^{-1} range. Because we believed that these lines were induced by boron doping, it seemed important to verify that they were present for other samples prepared with different growth conditions. Thus, a sample B was examined. It was grown in a National Institute for Research in Inorganic Materials, Tsukuba, Japan (NIRIM)-type reactor with B_2O_3 as a boron source. The plasma CVD reactor has already been described in ref. 13. Growth conditions were selected to obtain randomly oriented boron-doped diamond crystals on a Si substrate. Typical size of the diamond crystals was about 10 μm . Most of the crystals were of cubo-octahedral shape with little secondary nucleation. Grain boundary effects were studied at the boundary of three or more crystals. Sample

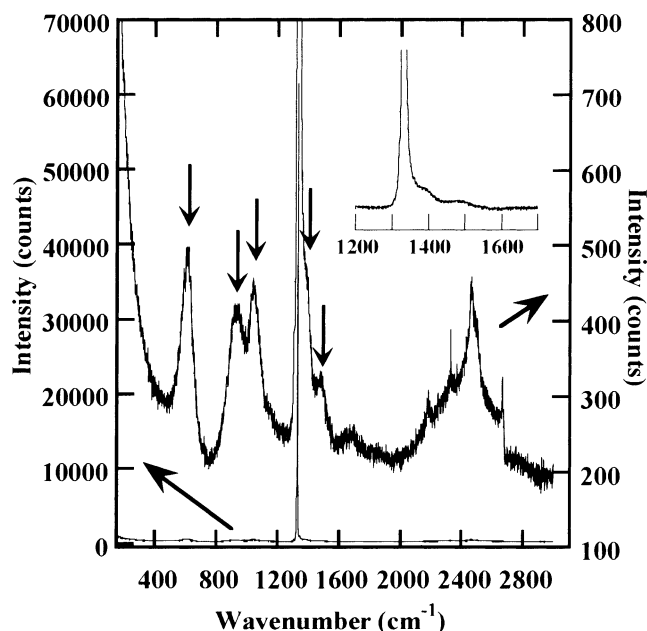


Figure 1. Example of Raman spectrum recorded for the NRL149 sample (sample A). The lower trace shows the full scale spectrum. Neither photoluminescence nor amorphous carbon peaks are detected. The higher trace shows a magnification of the spectrum. The second-order diamond Raman spectrum is observed in the 2000–2670 cm^{-1} range. The inset reveals asymmetry of the Raman diamond line.

B was examined without any specific treatment. Also used as reference samples were sample C, a high-pressure–high-temperature (HPHT) crystal; sample D, a natural diamond crystal (a faceted gem diamond); and sample E, undoped CVD diamond crystals grown in a NIRIM-type reactor.

Results

Single-Point Measurements: Typical Raman Spectra. The Raman analysis of the optically transparent diamond, sample A, was first conducted at random, keeping constant the spectrometer settings (optical alignment, laser power at the sample, and acquisition time) while probing different areas of the disk. Long acquisition times and the $\times 100$ microscope objective were first systematically used. The confocal aperture was adjusted to 200 μm to probe the sample's near-surface region.

A typical Raman spectrum from sample A is presented in Figure 1. It reveals an intense one-phonon diamond Raman line at ca. 1332 cm^{-1} with a peak width (fwhm) of 3.7 cm^{-1} . The line position is negligibly shifted from the line position for the reference diamond samples. Amorphous nondiamond sp^2 carbon phases are not detected on the growth side of the disk, but they are present on the substrate side of the disk, where the grain size is much smaller. The disk is clearly of high microstructural quality and contains relatively few defects based on the narrow diamond Raman line width. It is possible to detect minor asymmetry in the diamond line, in some regions, consistent with the presence of variable levels of boron in the lattice. This asymmetry, the so-called “Fano effect”,^{14–16} is undetectable unless the intensity axis is significantly magnified.

After enlargement, some interesting features appear at both low and high frequencies with respect to the diamond line. These features are quite distinct from those normally reported for heavily boron-doped diamond films or crystals.^{17–19} These latter are the broad lines centered near 550 and 1250 cm^{-1} . In the spectrum, there are three lower frequency peaks at 610, 925, and 1045 cm^{-1} . The intensity of these peaks tracks the level of

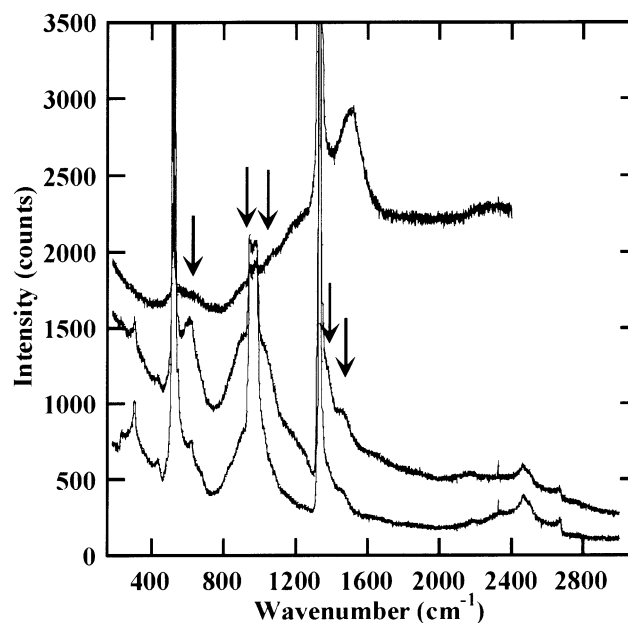


Figure 2. Example of Raman spectra recorded on particular boron-doped diamond crystals grown in a NIRIM-type reactor (sample B). The higher trace shows the spectrum recorded within the boundary of a few crystals. An amorphous carbon peak at 1500 cm^{-1} is clearly detected, superimposed on a photoluminescence background. The middle trace shows the spectrum recorded on a $\langle 111 \rangle$ face; the lower trace shows the spectrum recorded on a $\langle 100 \rangle$ face. The weak boron-related features are indicated by arrows. Other observable features are first- and second-order silicon Raman spectra at 520 and ~ 970 cm^{-1} . Note the Fano-like profile of the diamond line, especially for the spectrum recorded on a $\langle 111 \rangle$ face. The spectra have been displaced vertically for clarity.

“asymmetry” in the diamond line. There are also two higher frequency peaks at about 1375 and 1470 cm^{-1} . The former appears as a shoulder on the diamond line, and the latter occurs near the region (1500–1600 cm^{-1}) where broad scattering by amorphous nondiamond sp^2 carbon is often seen. The intensities of all five peaks are approximately only a few percent of the diamond line intensity, being comparable with the intensity of the second-order diamond features centered at ca. 2500 cm^{-1} .

For boron-doped diamond films, the asymmetry of the one-phonon diamond Raman line is generally attributed to a Fano-like interference. Indeed, as the boron concentration in the film reaches 10^{19} cm^{-3} and above, a Fano-like resonance is observed between a continuum of electronic states and the phonon energy. Such effects are well-known for Si and Ge semiconductors.¹⁴ However, a detailed examination of the spectrum presented in Figure 1 rather shows that one may describe the diamond line as being nearly symmetric with the apparent asymmetry resulting from the two higher frequency components cited above. Given the apparent lack of asymmetry in the line, the doping level may be estimated to be lower than the mid- 10^{19} cm^{-3} range.^{3,4,17,18} It should be mentioned, however, that the doping level threshold for the appearance of asymmetry in the diamond line varies somewhat from report to report. This is perhaps due to the challenges with using secondary ion mass spectrometry (SIMS) to quantify boron levels in doped films.²

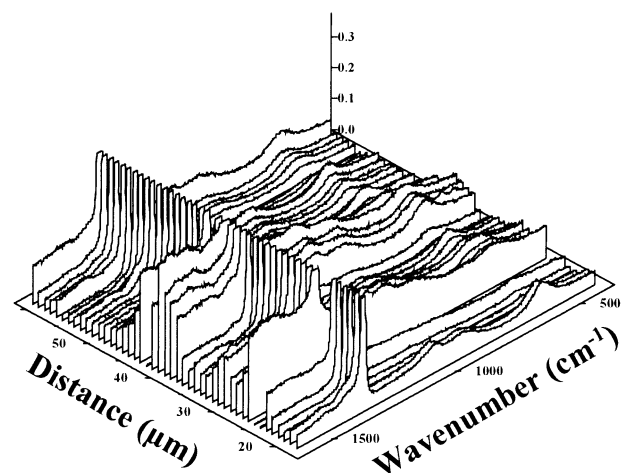
The same analysis protocol was followed when investigating sample B, the polycrystalline diamond film deposited on Si. Both $\langle 100 \rangle$ - and $\langle 111 \rangle$ -oriented growth facets were probed by focusing the laser beam on a single microcrystallite. Raman spectra recorded from each type of oriented microcrystallite and from a grain boundary between different microcrystallites are presented in Figure 2. Several features in the spectra from the

oriented microcrystallites unequivocally suggest a higher overall boron-doping level in this film compared to the optically transparent diamond disk. First, there is a strong decrease in the diamond line integrated intensity, even when using the same analysis conditions that were used to obtain spectra from the disk. This may indicate a more optically dense material due to a higher doping level. Second, all measured one-phonon diamond lines, regardless of the growth sector, exhibit asymmetry with an upward shift of the peak intensity on the high-wavenumber side. As expected, the asymmetry of the diamond peak is more pronounced for $\langle 111 \rangle$ facets because of the higher boron-doping level that is observed in this growth sector.^{3,4} In most cases, the diamond peak position is shifted somewhat with respect to the reference sample C, the HPHT diamond crystal. The line position is observed to vary slightly even within the same crystal. The line position variability is observed either as an increased shift (compressive stress) or as a lowered shift (tensile stress) of the peak. Such variability is not unexpected because if one local region is under compressive stress, then another region nearby must be under tensile stress. Hence, the diamond line position cannot be used as an indirect measure of the boron-doping level because of the influence of localized stress. The boron-doping level is estimated to be in the range of 10^{19} – 10^{20} cm⁻³ solely on the basis of the asymmetry of the diamond line.^{3,4,17,18} In general, the asymmetry is more obvious in spectra obtained from regions void of amorphous nondiamond sp² carbon inclusions. The nondiamond carbon phases were almost exclusively detected at the grain boundaries and in the regions where secondary nuclei formed on the primary diamond microcrystallites. The weak signals at 610, 925, 1045, 1375, and 1470 cm⁻¹ are also present in the spectra from this film, most noticeably in the spectra from the $\langle 111 \rangle$ - and $\langle 100 \rangle$ -oriented microcrystallites, that is, unobscured by the nondiamond-carbon scattering intensity and background PL. Their relative intensity, with respect to the diamond line intensity, is stronger than was observed for the optically transparent diamond disk because of the higher doping level. However, they strongly overlap with the first- and second-order Si Raman features.

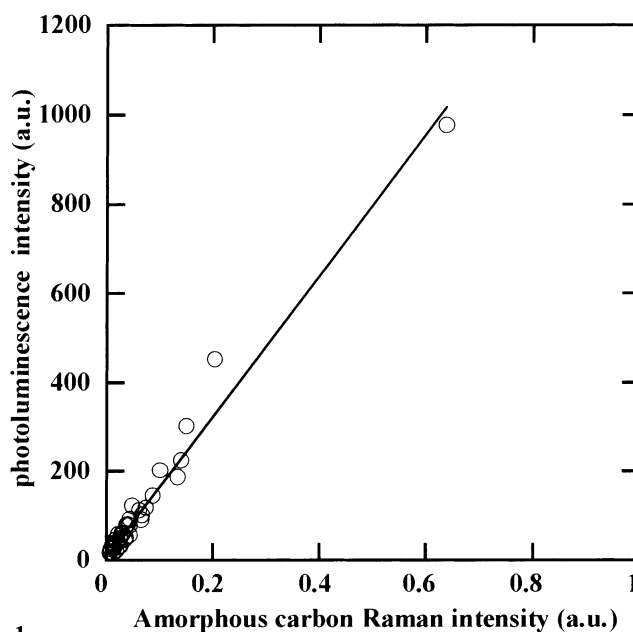
All of the additional peaks were observed regardless of the excitation wavelength (e.g., 514.5, 488.0, or 457.9 nm), which confirms that they result from Raman scattering. To the best of our knowledge, these weak intensity peaks have been mentioned in the literature only twice: once for the Raman analysis of boron-doped HPHT crystals²⁰ and another for CVD-grown epitaxial layers.²¹ The fact that these peaks are detected in both the polished optically transparent disk and the polycrystalline film indicates that the peaks do not result from a damaged layer produced by the mechanical polishing. It also appears that they cannot be assigned to impurities in the film that might be associated with the specific reactor used for the deposition. When depth-resolved spectra were acquired for the optically transparent diamond disk simply by varying the focal distance of the laser spot, no modification of the spectral line shape was detected. Therefore, we conclude that these weakly intense peaks are somehow related to the boron incorporated into the lattice.

As a side note, the detection of the second-order diamond Raman spectrum indicates the high quality of the microcrystallites in both films. In every case, the spectral features perfectly resembled those known for diamond. For a detailed description of the second-order features, one is referred to refs 22 and 23.

Line scans of Raman spectra were obtained from sample A, the optically transparent disk, to gain a more representative picture of the macroscopic microstructure. A representative set of spectra obtained over a 45 μ m linear distance is presented in



a



b

Figure 3. Raman spectra (a) obtained at 1 μ m intervals along a 45 μ m line for the sample A. Spectra have been normalized to the diamond line intensity. Full scale intensity axis is 10. Note the intensity variation of the weak intensity signals peaking at 610, 925, and 1045 cm⁻¹. Note also the background intensity variations. Panel b shows the correlation between the background intensity and the intensity of the broad line peaking at ca. 1500 cm⁻¹ assigned to amorphous carbon.

Figure 3a. The spectra were acquired at 1 μ m intervals along the profile. To improve the reading of the figure, all of the individual spectra have been normalized to the maximum diamond 1332 cm⁻¹ Raman line intensity in the series. The normalized spectra clearly reveal isolated regions of amorphous nondiamond sp² carbon phases on the basis of the broad scattering signal centered between 1500 and 1550 cm⁻¹. However, these phases were only detected if long acquisition times were used and the intensity scale was significantly enlarged. The second observable feature is the increase in the PL background intensity at the same isolated regions where the amorphous carbon (a-C) is detected. Hence, there is a linear correlation between the background PL intensity (measured at ca. 1700 cm⁻¹) and the scattering intensity by the amorphous nondiamond carbon phases, as is shown in Figure 3b. A similar correlation has previously been shown by us²⁴ and others.^{25–27} It suggests that much of the PL arises from absorption of the

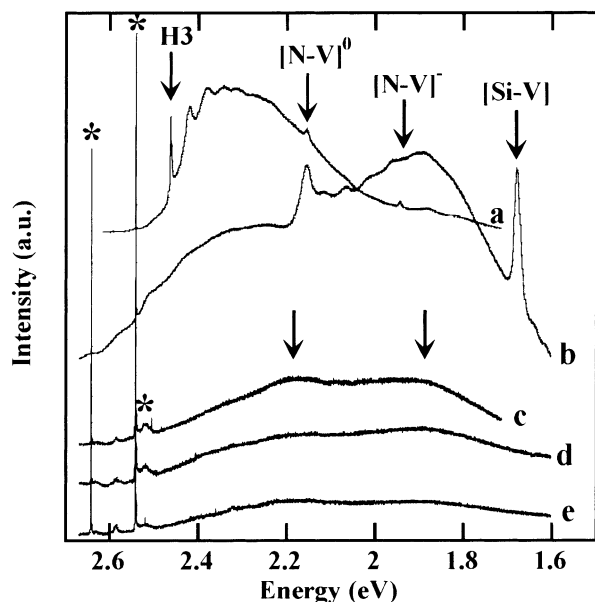


Figure 4. Comparison among the photoluminescence spectra, excited at 457.9 nm, of (a) HPHT diamond crystal and (b) undoped and (c,d,e) boron-doped CVD diamond crystals. Zero-phonon lines of H3, $[N-V]^0$, $[N-V]^-$, and $[Si-V]$ are indicated by arrows. Spectra c and d have been recorded on $\langle 100 \rangle$ and $\langle 111 \rangle$ faces, respectively; spectrum e has been recorded in a grain boundary region. Raman lines of the silicon substrate, amorphous carbon, and diamond are indicated by asterisks. Note the apparent increase in intensity of the two photoluminescence bands centered at ca. 1.9 and 2.2 eV with the incorporation of amorphous carbon. The spectra have been recorded at the liquid nitrogen temperature. They have been displaced vertically for clarity.

excitation light by localized amorphous nondiamond sp^2 carbon inclusions. However, it is known that a broad PL background can also be found underlying the N–V neutral and negatively charged centers at 2.154 and 1.945 eV, respectively. The actual nature of this PL signal must be analyzed in greater detail.

Single-Point Measurements: Photoluminescence Background. Figure 4 shows examples of PL spectra recorded for various diamond samples. The spectra were recorded at liquid nitrogen temperature using the 457.9 nm line from an Ar^+ laser. The spectra obtained for sample C, the HPHT (curve a in Figure 4), or sample E, the CVD undoped (curve b) reference diamond crystals, are similar in shape to those reported in the literature for similar crystals.^{11,28–32} Depending on the sample, the well-known nitrogen-related bands at 2.154 and 1.945 eV are observed along with the 2.46 eV peak (503 nm) assigned to the H3 center and the Si-related line at 1.681 eV. However, because of strain and disorder, the vibronic fine structure is not well-resolved for the CVD crystals. For sample E, a relatively wide band with line width ≈ 600 meV, centered at about 2.3 eV is also present in the spectrum. Similar wideband PL has been observed in both natural and synthetic diamonds^{11,25,27,33,34} and is sometimes referred to as band A luminescence.

From Figure 4, it can be observed that the low-temperature PL spectra for the CVD boron-doped crystals grown in the NIRIM-type chamber are completely different from the undoped sample spectra. The emission bands related to nitrogen or silicon or both disappear, likely because of lower boron states depopulating the ground states of these centers. The spectra are characterized by a broad signal from 2.4 to 1.6 eV. This signal appears to be composed of two distinct components centered at about 2.2 and 1.9 eV, respectively. Comparing the different spectra presented, it may be argued that this photoluminescent signal is actually correlated with the presence of nondiamond

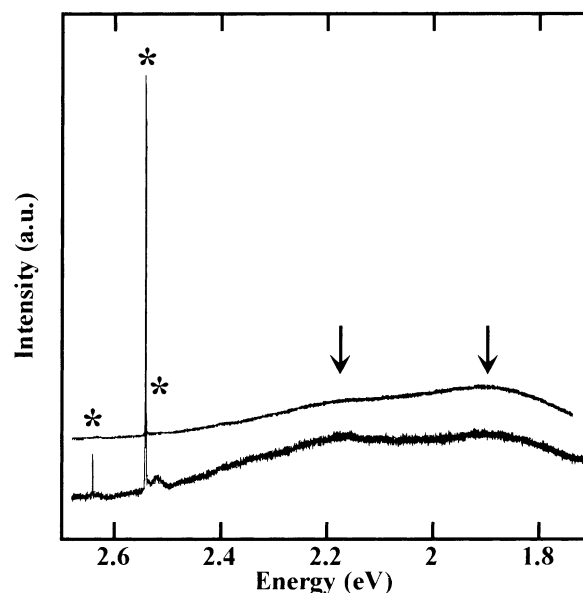


Figure 5. Comparison between the room temperature photoluminescence spectra, excited at 457.9 nm, obtained for the NRL149 sample, sample A (higher trace), and the boron-doped diamond crystals, sample B (lower trace). Raman lines are indicated by asterisks. The spectra have been displaced vertically for clarity. Arrows indicate the approximate position of the two photoluminescence bands.

carbon as the intensity increases proportionally with that of the broad a -C Raman signal peaking at 1500 cm^{-1} . This is consistent with some previously reported results.^{24–27}

Figure 5 compares the room-temperature PL spectra recorded for sample B and sample A. For sample A, the laser beam was focused on the same area probed during the line scan analysis. The spectra are similar in shape, even if the intensity ratio of the two bands varies from one sample to another. Note that the a -C Raman band at ca. 1500 cm^{-1} is hardly detectable for sample A, the optically transparent disk, which tends to indicate that the background PL intensity is more sensitive to the presence of nondiamond carbon than the Raman spectrum.

Finally, the five bands at 610, 925, 1045, 1375, and 1470 cm^{-1} are all present in each spectrum but not with the same intensity at each point along the line profile. In some cases, it becomes difficult to discriminate the peaks at 1385 and 1470 cm^{-1} from the Raman scattering by the amorphous nondiamond carbon inclusions. This observation further suggests that the level of boron incorporation is not uniform throughout the diamond sample.

Raman Imaging. Optical images, in both the reflection and transmission modes, from an $800 \times 600\text{ }\mu\text{m}^2$ area of sample A, the optically transparent diamond disk, are presented in Figure 6 (top and bottom left of the figure). In the center of each image, there is a $200 \times 400\text{ }\mu\text{m}^2$ region, highlighted in the box, that indicates where the Raman data were acquired. The resulting spectral maps are presented in Figure 6a–e. An objective lens of low magnification ($\times 10$) was first used, and because of the low numerical aperture ($na = 0.25$), the probing depth was high ($\geq 50\text{ }\mu\text{m}$). Under these conditions, the probing depth is mostly determined by the optical properties of the sample. Spectra were acquired with a $10\text{ }\mu\text{m}$ spacing using an acquisition time of 3 s per spectrum.

Figure 6a shows a false color representation of the transmission optical image. The bulk features present in the optical image are clearly apparent in the color image. The darker regions are more opaque and the brighter regions are more transmissive. Five different images have been constructed from the spectral

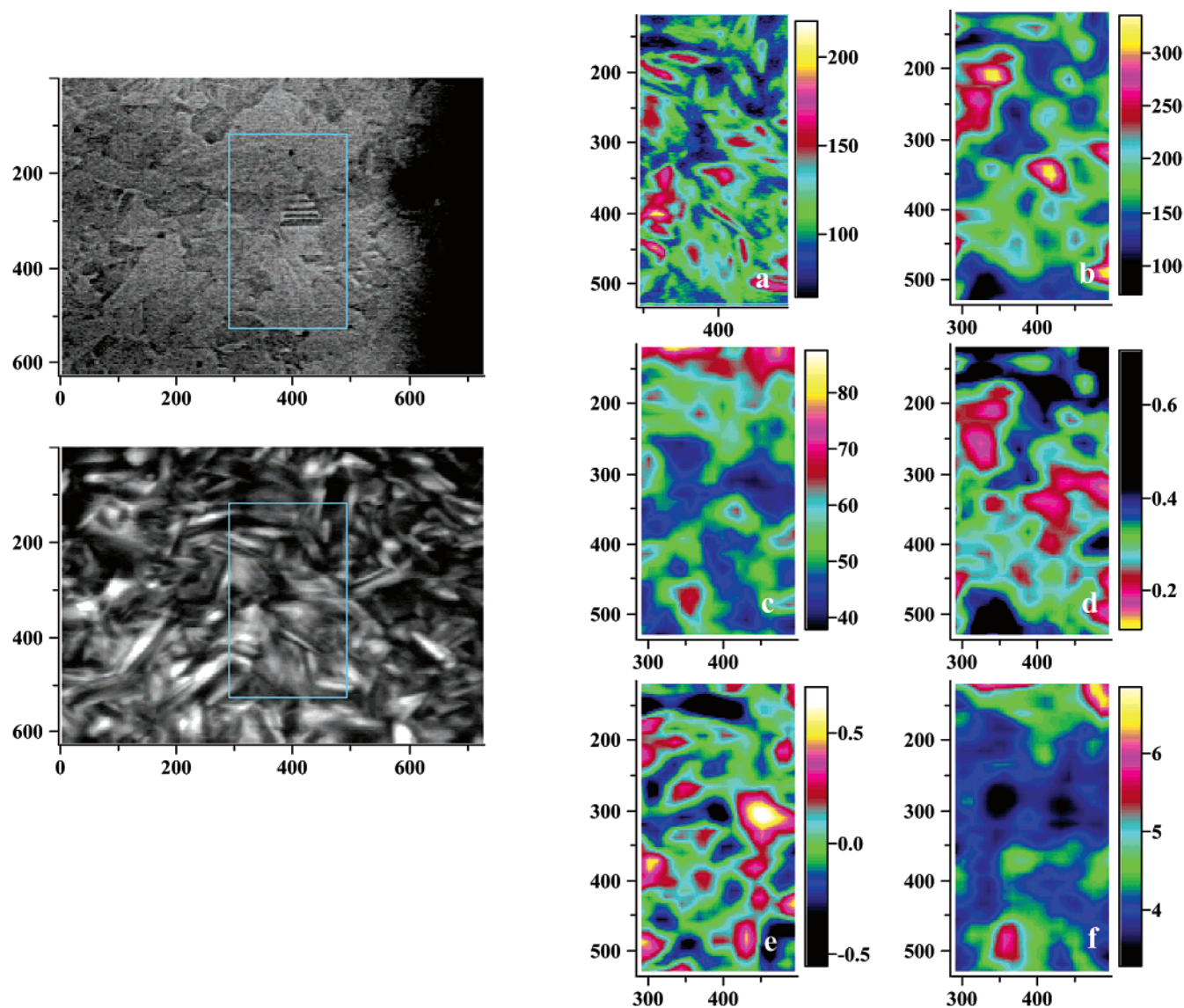


Figure 6. Optical (sample illuminated in reflection and in transmission) and Raman images obtained under low-magnification conditions ($\times 10$). For the optical images, the top panel shows a sample illuminated in reflection and the bottom panel shows a sample illuminated in transmission. The rectangle indicates the analyzed area ($200 \times 400 \mu\text{m}$). Panel a shows a false color representation of the transmission optical image, panel b the integrated intensity of the diamond line (arbitrary units), panel c the photoluminescence background intensity (arbitrary units), panel d the photoluminescence background intensity normalized to the diamond line position as a shift from 1332 cm^{-1} , and panel f the diamond line width. The diamond line frequency and width were obtained by fitting all of the individual spectra with a Lorentzian line shape.

data: (b) the integrated diamond line intensity, (c) the background PL intensity measured at 1650 cm^{-1} , (d) the ratio of the I_{1650}/I_{1332} intensities, (e) the diamond line position as a shift from 1332 cm^{-1} , and (f) the diamond line width. First, there are clearly some variations in the diamond line intensity from site to site (Figure 6b). The intensity distribution more or less resembles the false color optical image, although recorded with the rather low spatial resolution ($10 \mu\text{m}$). Thus, the diamond line intensity map partially reflects the local variations in the optical absorption coefficient. The regions of maximum line intensity approximately correspond to the regions with the larger transmissivity (i.e., larger sampling volume). Second, the background PL intensity is inhomogeneous over the area with no apparent correlation with the optical image features or the diamond line intensity (Figure 6c). Because the diamond line intensity is strongly related to local variations in the optical absorption coefficient, it is convenient to plot the ratio of the background PL intensity to the diamond line intensity to

normalize the scattering volume (Figure 6d). The map reveals that the regions of highest PL correspond to regions with the lowest diamond line intensity and the highest optical density. Some of the reasons for the higher optical density could be light scattering by defects, inhomogeneous boron doping, and *a*-C impurities. Already in Figure 3, we showed a direct correlation between the PL intensity and the scattering intensity by nondiamond sp^2 carbon inclusions. However, the results must be interpreted with some caution because loss of intensity of the diamond line may be related to other causes, in particular, with the different instrument response with respect to the polarization of the scattered radiation, but nevertheless, the trends are still present.

Third, there is some shift in the diamond line position over the imaged area but the overall magnitude of the shift is less than 1 cm^{-1} (Figure 6e). To the first approximation, an increased Raman shift reflects compressive stress and a decreased shift reflects tensile stress. There are clearly regions in which the

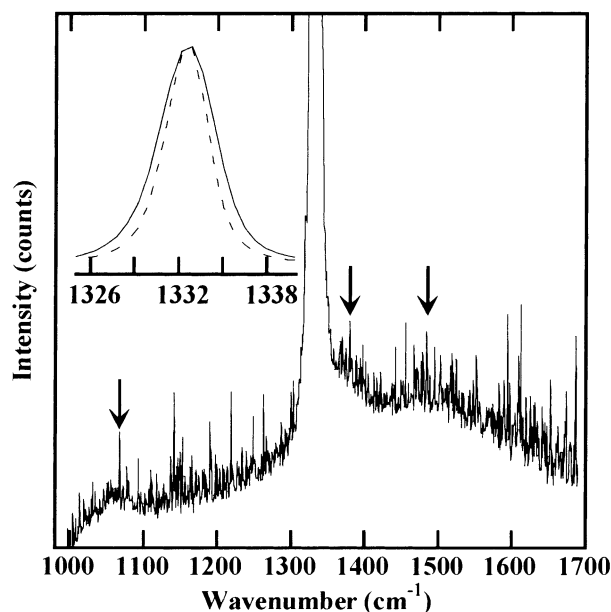


Figure 7. “Macro-Raman” spectrum of the NRL149 sample obtained by averaging all of the spectra used to construct the images presented in the Figure 6. Arrows indicate the weak Raman features. The inset shows the sample (full line) and HPHT reference crystal (dashed line) diamond line profiles.

stress state is compressive (red and yellow colors) and nearby regions where the stress is tensile in nature (blue and black colors). Both of these areas have dimensions of some tens of micrometers. There is reasonable correlation between the regions of maximum upward shift and highest optical transparency, largest diamond line intensity, and lowest PL intensity. For all of the spectra, the diamond line was symmetrical (to the first approximation because we did not take into account of the 1385 cm^{-1} component) and has been curve-fitted with a Lorentzian line shape. The data also suggest that boron doping does not induce a downshift of the diamond line. Fourth, for about 60% of the spectra, the diamond line width is lower than 4 cm^{-1} (Figure 6f). A 3.0–3.2 cm^{-1} line width was measured for an undoped HPHT diamond reference crystal using the same spectrometer settings. The regions where the diamond line width is largest, as indicated by the red and yellow colors, are the nearly same regions where the PL intensity is largest. We have already indicated a correspondence between the PL intensity and scattering intensity by nondiamond sp^2 carbon. It is such *a*-C regions where microstructural disorder is expected to be the most significant.

Figure 7 shows a useful comparison between the average Raman spectrum obtained from the entire $200 \times 400 \mu\text{m}^2$ imaged area of sample A and that of sample C, the undoped HPHT diamond reference crystal. Within the experimental accuracy (estimated to be $\pm 0.03 \text{ cm}^{-1}$ with the current spectrometer settings), the diamond line for the disk is unshifted with respect to the reference crystal (see insert). So for all practical purposes, the film is macroscopically unstressed. On the other hand, there is a slight broadening of the line, $\sim 1 \text{ cm}^{-1}$, as compared to the reference crystal. This line broadening mostly reflects the frequency variations over the analyzed area. The average spectrum also exhibits some slight asymmetry of the diamond line and weak features at 1045, 1375, and 1470 cm^{-1} . Unfortunately, the S/N ratio of the former peaks was too low to allow their use in the construction of spatial maps.

In summary, (i) the optically transparent diamond disk is of high quality, low in microstructural defects, (ii) it macroscopi-

cally contains minor stress, (iii) the diamond line can be represented by a nearly symmetric line shape, which indicates that the boron-doping level is below the threshold value (ca. $5 \times 10^{19} \text{ cm}^{-3}$) for which a Fano-like line deformation is typically distinguished, and (iv) there are some variations in the local optical properties, as evidenced by the maps of the diamond line and PL intensities.

The data presented reflect the bulk film properties. The electrochemical behavior of an electrode, in addition to being a function of the bulk material properties, is also a function of the surface microstructure. To probe the surface microstructure of diamond electrodes, it is necessary to use a high numerical aperture objective lens.

A second set of measurements was thus performed on sample A, the optically transparent diamond disk, using a $\times 100$ objective lens and confocal aperture of $200 \mu\text{m}$ in an effort to confine the probed volume to the near-surface region. Three different regions were probed over a $20 \times 40 \mu\text{m}^2$ area with a point spacing of $0.7 \mu\text{m}$. Also, different excitation wavelengths of 514.5 and 457.9 nm were used. All of the optical images at this magnification were featureless, reflecting the smoothness of the polished disk. One example will be described below. However, independent of the sample area analyzed, the same trends and conclusions were obtained.

Figure 8 shows a series of spectral maps including (a) the integrated diamond line intensity at 1332 cm^{-1} , (b) the PL intensity at 1650 cm^{-1} , (c) the integrated line intensity at 1045 cm^{-1} associated with the boron dopant atoms, (d) the I_{1045}/I_{1332} ratio, (e) the diamond line position as a shift from 1332 cm^{-1} , and (f) the diamond line width. First, the spatial distribution of the diamond line intensity allows one to clearly distinguish the large grains (Figure 8a). The line intensity varies by over a factor of 2. Second, the background PL intensity arises almost exclusively from some of the grain boundaries (Figure 8b). These boundaries are only defined by one or two pixels in the image. It is interesting that the PL intensity is not detected from all of the grain boundaries. For example, the boundaries between the crystal of rectangular shape, located at the bottom of the image, and the nearby crystals are luminescence-free. This is a strong indication that the atomic structure of the different grain boundaries is different and possibly depends on the relative orientation of the diamond crystals. This observation was common for the different regions of the disk probed. Third, the intensity of the 1050 cm^{-1} line was high enough to be fitted by a mixed Gaussian–Lorentzian line shape (Figure 8c). It is clear that the boron distribution is not homogeneous over the probed region. The regions of the highest intensity exhibit the least intense diamond line intensity, that is, the more optically dense regions. These different sectors perfectly correspond to the individual grains. Fourth, the variations in boron signal intensity are nicely visualized in the I_{1045}/I_{1332} map (Figure 8d). This figure interestingly shows that there are even apparent variations in the boron signal within the same grain. Fifth, there are significant variations of the diamond line frequency shift from region to region (Figure 8e). The shift ranges over $\pm 4.8 \text{ cm}^{-1}$, even if most of the data are shifted by ca. $\pm 2 \text{ cm}^{-1}$. For about 10% of the individual spectra, line splitting into two or more components was clearly observed. The larger crystals, which can easily be recognized in the diamond line intensity image (labeled 1, 3, and 4 in Figure 8d), are clearly in compression. Small frequency variations are also present for smaller grains located on the right-hand side of the image. In particular, the stress state for the lower grain or subgrain is slightly tensile. The maximum upshift of the diamond line is observed at the

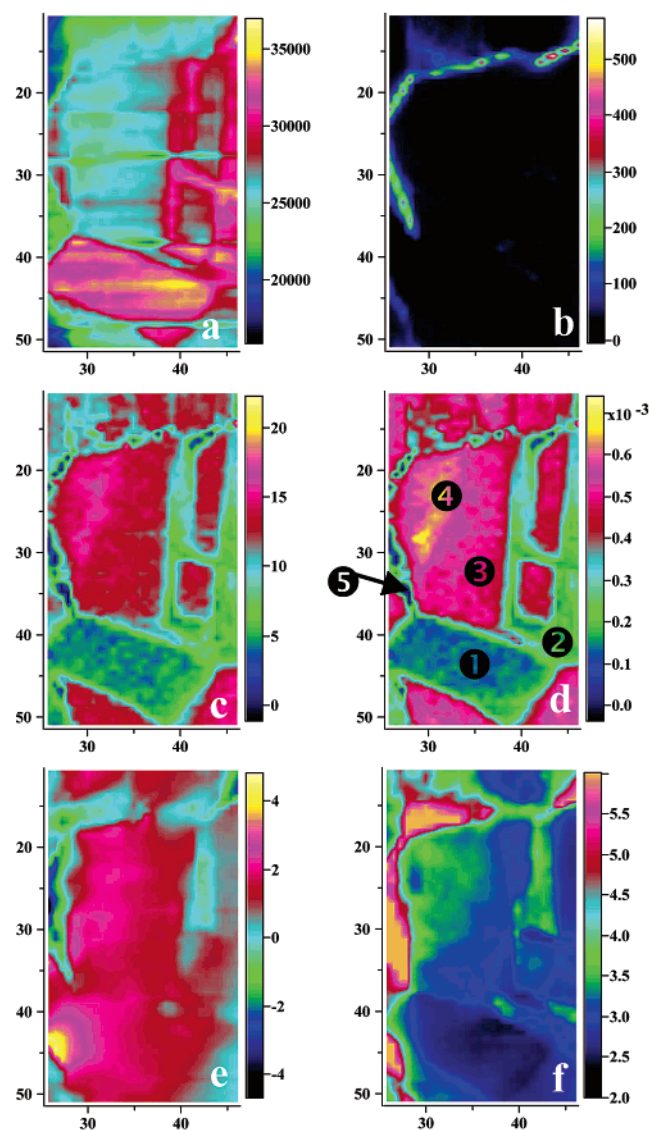


Figure 8. Examples of confocal Raman images obtained over a $20 \times 40 \mu\text{m}$ probed area: (a) integrated intensity of the diamond line (arbitrary units); (b) photoluminescence background intensity (arbitrary units); (c) integrated intensity of the 1045 cm^{-1} line (arbitrary units); (d) intensity ratio of the 1045 cm^{-1} peak to the diamond line; (e) diamond line position (cm^{-1}) as a shift from 1332 cm^{-1} ; (f) diamond line width (cm^{-1}). Horizontal striations observed in panel a are due to a slight instrument instability during the acquisition. The diamond line frequency and width were obtained by fitting all of the individual spectra with a Lorentzian line shape. Five different regions are indicated in panel d. Their average spectra are compared in Figure 9.

boundary of three different crystals (yellow region in the figure), while the maximum downshift is clearly observed within the photoluminescent boundaries. The significant frequency variations are observed over very short distances, typically over micrometer dimensions. Sixth, strong variations of the diamond line width are also observed (Figure 8f). The first remarkable result is that, locally, some of the diamond grains appear to be high quality, the diamond line width being slightly lower than that observed for the undoped HPHT diamond reference sample. Second, the imprint of the grains and the luminescent boundaries are still detected on the diamond line width image. The diamond line width image is also found to partially correlate with the 1045 cm^{-1} line intensity image, that is, a larger line width is observed in some regions where the boron-related signal is most intense. However, this correlation is fortuitous, as evidenced

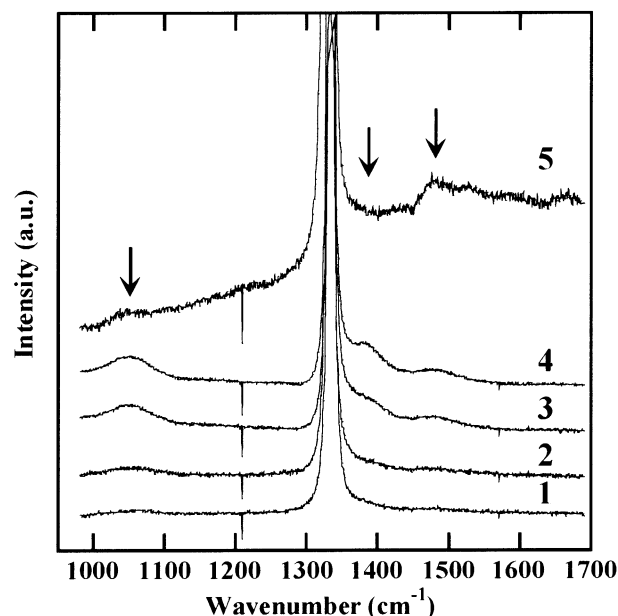


Figure 9. Raman spectra obtained for different regions of the Raman images presented in Figure 8d. Arrows indicate the frequency of the bands peaking at 1045 , 1375 , and 1470 cm^{-1} . The notch at $\sim 1210 \text{ cm}^{-1}$ is an artifact.

by the upper and the lower part of both images. The areas with the largest peak width are the same as those with the most intense background scattering. For these regions, broadening is systematically induced by the splitting in two or even more components of the diamond line. Thus, this broadening appears mostly stress-induced and cannot be explained by confinement effects induced by a strong decrease of the coherent domain size.

Average spectra have been constructed in Figure 9 for the different sectors that are labeled from 1 to 5 in Figure 8d. Averaging a high number of spectra (~ 100) greatly improves the S/N ratio. Comparing the representative spectra, it is evident that the 1045 cm^{-1} line intensity strongly correlates with the 1375 and 1470 cm^{-1} line intensities, indicating that they may have a common origin.

A large number of spectra recorded along the grain boundaries are also available, and representative spectra extracted from the luminescent areas are presented in Figure 10. It is worth noting that there is no single characteristic spectrum for the luminescent grain boundaries. In some cases, the usual broad signal characteristic of aromatic and graphite-like sp^2 phases is observed, see, for example, the second spectrum from the top in the figure. However, in most cases, several relatively sharp and weak peaks are observed in the $1100\text{--}1700$ wavenumber range. Obviously, the width of these peaks is too small to be assigned to any specific amorphous sp^2 phase. They were observed regardless of the excitation wavelength, which confirms that they result from Raman scattering. Thus, these peaks have to be associated with specific defect structures that are present within the crystal boundaries. Similar weak Raman signals have been observed for ion beam implanted diamond,^{35–37} and it is thought that some of them may arise from localized bonding between 3-fold and 4-fold coordinated carbon atoms. Finally, for most of the spectra in Figure 10, the presence of the 1045 cm^{-1} line is questionable, suggesting boron depletion at the photoluminescent boundaries. However, the line shape of some of the spectra may still indicate the presence of boron, see the upper spectrum in the Figure 10 for which a weak Fano-like profile may be discussed. From these observations, it

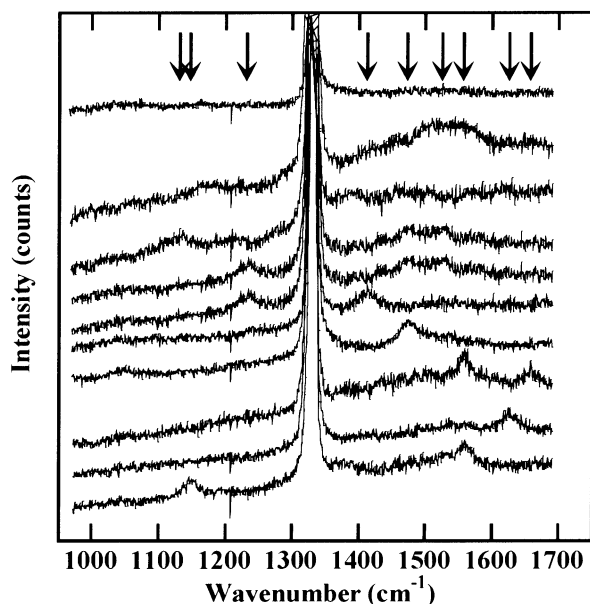


Figure 10. Examples of spectra extracted from the “image” file along the photoluminescent grain boundaries. Arrows indicate all of the weak features that can be distinguished on the spectra. The notch at $\sim 1210\text{ cm}^{-1}$ is an artifact.

appears impossible to give a simple and unique description of the crystal boundaries.

The above images reveal that a microscopic picture of the diamond film microstructure, relative boron-doping level, PL, and internal stress can be developed from Raman spectral maps. Finally, a fourth region of the disk was analyzed using the high-dispersion mode of the spectrometer. Because of the lower spectral range available with this mode (200 cm^{-1} , see the experimental part), most of the information regarding the nondiamond carbon content and the relative boron-doping level is lost, but a more detailed examination of the diamond line profile is possible. Some results are presented in Figure 11 in the form of $25 \times 40\text{ }\mu\text{m}^2$ maps. The images shown are the (a) integrated diamond line intensity, (b) PL intensity, (c) integrated intensity of the boron-related 1375 cm^{-1} line, (d) I_{1375}/I_{1332} ratio, (e) diamond line position as a shift from 1332 cm^{-1} , and (f) diamond line width. First, the integrated diamond line intensity image is presented using a gray scale representation, which reveals five different crystals (Figure 11a). It can be seen that within two of the crystals there are strong diamond line intensity variations, which may be indicative of the presence of subgrains or growth sectors separated by twins.³⁸ It is likely that the contrast of the diamond line intensity image partially results from differences in the boron concentration or from orientation differences among the various grains. Because the laser is linearly polarized and the gratings have a strong polarization dependence, such intensity variations are not unexpected. Second, all of the crystals in this image are separated by photoluminescent crystal boundaries, as seen the background map (Figure 11b). The integrated diamond line intensity was determined by fitting the peak for each of the individual spectra using a Lorentzian line shape. A second line was introduced into the line-fitting procedure to take into account the weak boron-related peak at ca. 1375 cm^{-1} , which is the only boron-related feature available within the analyzed spectral range. However, this fitting procedure induced artifacts along the grain boundaries because part of the signal arising from nondiamond phases is artificially introduced in this second component. Thus, along the crystal boundaries, the 1375 cm^{-1} line intensity is

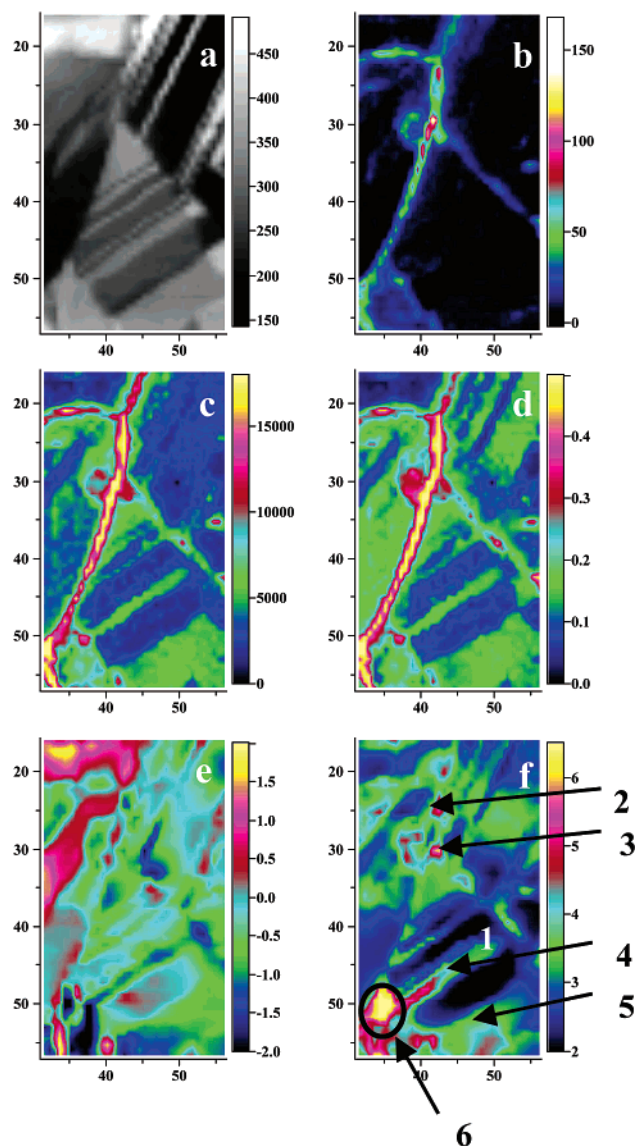


Figure 11. Confocal Raman images obtained over a $20 \times 40\text{ }\mu\text{m}$ probed area, using the high-dispersion mode of the spectrometer: (a) integrated intensity of the diamond line (arbitrary units); (b) photoluminescence background intensity (arbitrary units); (c) integrated intensity of the 1375 cm^{-1} line (arbitrary units); (d) intensity ratio of the 1375 cm^{-1} peak to the diamond line; (e) diamond line position (cm^{-1}) as a shift from 1332 cm^{-1} ; (f) diamond line width (cm^{-1}). The diamond line frequency and width were obtained by fitting all of the individual spectra with a Lorentzian line shape. In panels c and d, the contrast observed along the grain boundaries is an artifact induced by the fitting procedure, see the text. Arrows indicate areas where individual spectra (Figure 12) were recorded.

over-estimated and will not be considered in the following. As well as for the preceding example, it is seen from the I_{1375}/I_{1332} ratio image that the boron concentration is not homogeneous over the analyzed area. Moreover, it is remarkable to continue to find the imprint of growth sectors related by twins on this image.

For about 30% of the individual spectra obtained in the imaged area, the diamond line could be accurately represented by a single Lorentzian component. However, the most common line shape was one with some asymmetry. Also, in nearly half of the spectra, the diamond line was clearly split into two or more components. Examples of such spectra are presented in the Figure 12. The spectra are numbered according to the region

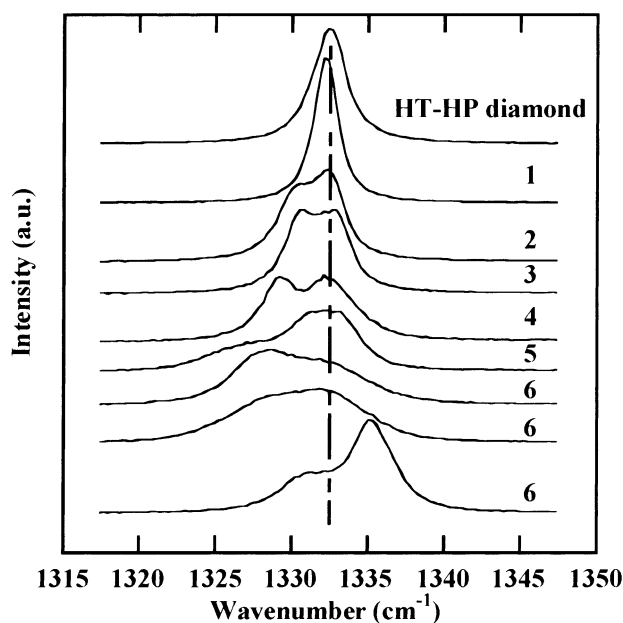


Figure 12. Some typical individual Raman spectra extracted from the "image file" (Figure 11). Spectrum 1 is typical of a nearly strain-free region and has to be compared to the reference spectrum obtained for a HPHT diamond crystal. Other spectra correspond to strained regions.

of the image they were obtained from, as shown in in Figure 11f. They are compared to that of sample C, the reference HPHT crystal. From the figure, it is first observed that the diamond line width may be smaller than that of the reference crystal, confirming the high quality of some crystals of the film. The other examples show spectra for which at least two components are needed to represent the line profile. For instance, two distinct components were observed at 1331 and 1335 cm^{-1} (lower trace in the Figure 12). For such a case, the first component is downshifted and the second upshifted from the position measured for the reference sample. In principle, the magnitude of the splitting (frequency difference of the different peaks) of the diamond line may be considered as a measure of stress. However, these double peaks rarely satisfy the correlation between absolute peak shift and splitting required by theory.^{39,40} Moreover, such calculations can be undertaken only for the particular case for which the crystal orientation and the measurement conditions are well-known, which is not the case here. Thus, line splitting can only be considered as the experimental evidence of nonhydrostatic stress within individual crystals. The same overall contrast is more or less observed on the diamond line width image: it is still possible to identify all of the crystals and grains that are detected on the diamond line intensity image. There are some areas for which the line width is $<2 \text{ cm}^{-1}$ (black areas in the figure). For most of the other areas, line splitting is observed. Thus, the diamond line width reflects the strain that is present within the probed volume. The frequency image is once again strongly contrasted ($\pm 2.5 \text{ cm}^{-1}$), and it appears that there are hardly any stress-free regions. There is still tensile stress detected along the crystal boundaries, but this is not a general rule. Stress sign and magnitude differences are observed at each of the grain boundaries. On the basis of these results, one can think that the observed stress is due to the presence of structural defects, in particular grain boundaries.

Discussion

The results presented herein first emphasize the amount of variability that can be seen in the microscopic spectra of CVD

diamond, although the macro-Raman spectra of such films can appear reproducible. In particular, they confirm that the crystal or film quality cannot be assessed in view of a few single-point measurements. Some of the foregoing results also show that the picture that emerges from a Raman analysis of such films strongly depends on the scale of observation of the sample: to get representative data of a sample (bulk data), the probing beam needs to illuminate a representative area of the sample, that is, the laser spot has to be much larger than the average grain size.

The variability within the boron-doped disk mostly derives from its polycrystalline nature. The above images reveal that a microscopic picture of the diamond film microstructure, relative boron-doping level, PL, and internal stress can effectively be developed from Raman spectral maps. However, as evidenced by the foregoing, it is difficult to give a simple description of the sample near-surface region in terms of microstructure. Nevertheless, it is possible to extract some trends from these results.

The first trend is the high perfection of some of the growth sectors of the diamond disk. The diamond Raman line width was often observed to be more narrow than that of the crystals considered as references in this study. Locally, that is, for particular areas of a few tens of square micrometers, values as low as 1.9 cm^{-1} have been measured using the high-dispersion mode of the spectrometer. Such a value is close to the lowest known value for HPHT synthetic diamond (1.5 cm^{-1}), and may be compared to $2.2\text{--}2.8 \text{ cm}^{-1}$ line widths usually observed for IIa- or Ia-type natural diamonds. The larger line width observed for the other crystals of the film is attributed to stress effects. Despite its high quality, the film is far from being strain-free. Lattice strain, or the stress which causes it, is evidenced by the position and (or) splitting of the triply degenerate diamond Raman line. Locally, the average line shift may be as high as $\pm 4.8 \text{ cm}^{-1}$, meaning that stress tensor components are in the GPa range. The grain boundaries are the first source of stress. However, they are not all equivalent: some of them present a weak PL background that can be assigned to the presence of *a*-C or specific defects, which were evidenced by weak Raman lines peaking in the $1100\text{--}1700 \text{ cm}^{-1}$ range. In such a case, this stress often appears as tensile, but this is not a general rule. The second observed scenario is that with a strong stress variation in the sign and magnitude of stress on both sides of the grain boundary, as if locally there was a mechanical balance. The third situation is the one with a continuous stress field through two neighboring crystals. In such a case, there is a very smooth change in the appearance of the spectrum between adjacent points with $0.7 \mu\text{m}$ spacing. An example for which these last two situations were observed within a few micrometers is presented in the Figure 13. Thus, stress fields across grain boundaries cannot be described in a simple way. The nature of the chemical bonding (sp^2 or sp^3) inside the boundary and especially the misorientation between neighboring crystals should be at the origin of the observed results. Note that planar defects, twin planes in particular, have also been identified to be a source of stress. The last characteristic of this film is the striking absence of PL that can be generated using a visible light. In particular, we were unable to detect any PL signal monitoring the presence of nitrogen within the crystals or the film. For this particular sample, this is perhaps not an unexpected result because this film was grown using high-purity conditions. However, such clean conditions were not used for the growth of the other boron-doped sample; for assurance, see the comparison between the PL spectra b and c-e presented in Figure 4. The lack of any observed N-V (and Si-V) complexes

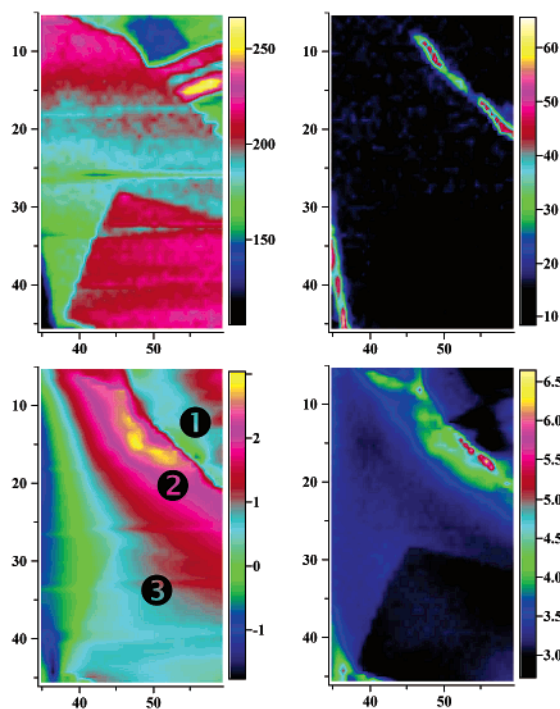


Figure 13. Confocal Raman images obtained over a $20 \times 40 \mu\text{m}$ probed area: (a) integrated intensity of the diamond line (arbitrary units); (b) photoluminescence background intensity (arbitrary units); (c) diamond line position as a shift from 1332 cm^{-1} ; (d) diamond line width. Different stress evolutions over grain boundaries are observed; see the frequency evolution between areas 1 and 2 (steep evolution of the stress sign on both sides of the grain boundary) and areas 2 and 3 (progressive and continuous stress evolution on both sides of the grain boundary). No attempt to extract the boron content has been undertaken.

in the spectral range studied may first result from the competition of the boron impurities with the vacancies. Indeed, all of the photoluminescent centers involve both nitrogen atoms and vacancies, and some studies have shown that boron doping dramatically reduces the vacancy content in CVD diamond films.⁴¹ It may also result from a downshift of the Fermi level upon doping, leading to changes in the occupations of the defect centers.³² PL signals have been detected within some of the grain boundaries. This luminescence is associated with the presence of nondiamond carbon. Broad green and red bands peaking at ~ 2.2 and ~ 1.9 eV have been detected, in agreement with some of the available data.

The doping level of sample A is not high enough to induce a strong Fano-type deformation of the Raman spectrum. From comparison with the available data, the average doping level of sample A may be estimated to be in the low- to mid- 10^{19} cm^{-3} range. However, by closely examining spectra, weak signals peaking at about 610, 925, 1045, 1375, and 1470 cm^{-1} were evidenced. In this study, these signals were also observed from CVD boron-doped crystals, which were obtained using different synthesis reactors and doping methods. They were also partially mentioned previously.^{20,21} Because these signals were observed only for boron-doped crystals, it is plausible to believe that they originate from boron incorporation within the diamond lattice. Their presence in the spectra has allowed us to infer images of the boron distribution at the near-surface of the sample. As expected, this distribution is not homogeneous but in general reflects well the various growth sectors in the film. One finds here that boron incorporation in the diamond lattice is a strong function of the crystalline orientation of the growth surface and possibly of the specific mechanism of growth, for

example, step flow versus island nucleation. For the moment, we cannot give satisfactory explanations for the origin of these bands. They have been observed for different excitation wavelengths, confirming that they are due to Raman scattering. There are three possible explanations of these lines.

(i) Localized Vibrational Modes of Boron. Such modes are observed for heavily boron-doped silicon, $> 10^{19} \text{ cm}^{-3}$.⁴² Boron, being a lighter atom than silicon, produces a local vibrational mode that occurs at a frequency higher than that of the optical phonon (520 cm^{-1}). Because of isotopic effects, two weak structures on the decreasing tail on the high-frequency side of the Si optical phonon are observed at 620 cm^{-1} for ^{11}B and 644 cm^{-1} for ^{10}B with an intensity ratio of 4:1, which reflects the natural abundance of the two isotopes. Thus, according to this hypothesis, two modes are expected at the high-frequency side of the diamond optical phonon. On the other hand, boron, which is lighter than carbon, should not form local modes in a wavenumber range lower than the phonon line of diamond. The 1375 and 1470 cm^{-1} lines possibly can be interpreted according to this scheme, which is not the case for the lines peaking in the $500\text{--}1100 \text{ cm}^{-1}$ wavenumber range.

(ii) Defects-Induced Spectra. Because of the presence of lattice defects, the translational symmetry is lost. The consequence is that the $k \approx 0$ selection rule is no longer valid so that phonons throughout the Brillouin zone can contribute to first-order Raman scattering. Such an assumption was already advanced to explain the appearance of broad lines peaking at about 550 and 1250 cm^{-1} , commonly observed for the most heavily doped samples, 10^{20} cm^{-3} and higher,^{2-5,17-19} or even for nanocrystalline diamond crystals,^{36,43} that is, for samples for which the coherent domain size is limited to a few tens of angstroms. In the same spirit, it is interesting to note that defect-induced first-order infrared spectra are effectively observed for boron-doped diamond crystals.⁴⁴ They exhibit several broad features in the $1000\text{--}1600$ wavenumber range, some of them more or less matching the observed Raman frequencies. Note also that the Raman-allowed but infrared-forbidden zone-center optical phonon is also observed in these infrared spectra. It is also observed that the presence of boron in concentrations as low as 10^{16} cm^{-3} can produce an observable effect on the infrared spectra. Thus, the possibility of an analogous effect on the Raman spectra cannot be ruled out. However, it is necessary to admit that such a spectrum should be impurity-specific. In the analogous case of diamond with nitrogen impurities, a one-phonon infrared spectrum can indeed be observed along with the zone-center optical phonon line. However, its line shape is different from the case of boron-containing diamond. Moreover, the Raman spectra of such samples do not exhibit other features than the allowed Raman line.

(iii) Electronic Raman Scattering. As well as for boron-doped silicon,⁴⁵ electronic Raman scattering has effectively been observed in boron-doped diamond.⁴⁴ However, the Raman transition has been observed at ca. 15 cm^{-1} and for temperatures lower than ca. 200 K . In the aforementioned studies, no other signals have been detected so far.

Thus, at this stage, it is still not clear whether these lines are due to local modes, defects, or electronic transitions or even to a combination of these different origins. So as to understand the origin of these signals, it thus appears necessary to undertake a specific study of sample obtained for a wide range of boron concentration. Such a study has to include the polarization, temperature, and isotopic composition dependence of these signals. This work is currently in progress.

We already mentioned that the long-term goal of our work with optically transparent diamond disks is to develop usable electrodes for spectroelectrochemical measurements in the UV/vis/IR regions of the electromagnetic spectrum. It remains also to understand how the local variations of the electrode microstructure can affect the electrochemical response of the electrode. Thus, part of the future work regarding these electrode has to include the study of the local electrochemical properties of such samples. This work is also in progress.

Conclusion

The first objective of this work was to use Raman and PL imaging to investigate the structural and chemical inhomogeneities that exist in a self-supported, optically transparent, boron-doped diamond disk.

First, unusual boron-related weak Raman features were detected in the 500–1500 cm^{-1} spectral range. At this stage of the study, it is still not clear whether these lines are due to local modes, defects, electronic transitions, or even to a combination of these different origins. However, their presence in the spectra has allowed boron maps within the film to be obtained.

It is confirmed that boron is incorporated in CVD diamond films with some inhomogeneities. Qualitatively, the boron concentration maps reveal the imprints of grains or subgrains. The characteristics of this sample, low roughness and large grain size, have also allowed a detailed analysis of the grain boundaries to be made. Some of the grain boundaries are found to incorporate *a*-C or specific defects evidenced by weak Raman signals in the 1100–1700 cm^{-1} range. However, this is not a general rule. The presence of nondiamond carbon within the grain boundaries is also revealed by a slight increase of the PL background. In such a case, the photoluminescent background seems more sensitive to the presence of *a*-C than the Raman analysis itself. Some of the measurements tend to indicate boron depletion at the grain boundaries, but this is not a general rule.

Despite its high quality, the film is far from being strain-free. Large stress variations are observed over micrometer dimensions. Strain, as revealed by the diamond line shift or splitting, has been observed along planar defects and grain boundaries. However, on the basis of these results, it is still impossible to understand the origin of the high compressive stress observed in some particular crystals of the film.

Finally, it should be pointed out that confocal micro-Raman spectroscopy (and PL spectroscopy), when used with appropriate mapping stages, are very efficient tools to characterize samples that present heterogeneities at the micrometer scale. It is obvious that, when single-point measurements are used, a great part of the information regarding the sample is missing.

Acknowledgment. G.M.S. acknowledges the financial support provided by the National Science Foundation—Analytical and Surface Chemistry program and the Department of Energy—Office of Basic Science. The summer fellowship provided by INPG is also greatly appreciated. A. Crisci (CMTC/INPG) was of great assistance in obtaining the data.

References and Notes

- (1) Burns, R. C.; Cvetkovic, V.; Dodge, C. N.; Evans, D. J. F.; Rooney, M.-L. T.; Spear, P. M.; Welbourn, C. M. *J. Cryst. Growth* **1990**, *104*, 257.
- (2) Steeds, J. W.; Gilmore, A.; Charles, S.; Head, P.; Howarth, B.; Butler, J. E. *Acta Mater.* **1999**, *47*, 4025.
- (3) Ushizawa, K.; Watanabe, K.; Ando, T.; Sakagushi, I.; Nishitani-Gamo, M.; Sato, Y.; Kanda, H. *Diamond Relat. Mater.* **1998**, *7*, 1719.
- (4) Ushizawa, K.; Nishitani-Gamo, M.; Watanabe, K.; Sakagushi, I.; Sato, Y.; Ando, T. *J. Raman Spectrosc.* **1999**, *30*, 957.
- (5) Wang, Y.; Li, H.; Xiong, Y.; Zhang, S.; Lin, Z.; Feng, K. *Diamond Relat. Mater.* **2000**, *9*, 1708.
- (6) Huang, J. T.; Hu, C. S.; Hwang, J.; Chang, H.; Lee, L. *J. Appl. Phys. Lett.* **1995**, *67*, 2382.
- (7) Sahli, S.; Aslam, D. M. *Appl. Phys. Lett.* **1997**, *70*, 2129.
- (8) Wang, J.; Swain, G. M.; Mermoux, M.; Lucazeau, G.; Zak, J.; Strojek, J. W. *New Diamond Front. Carbon Technol.* **1999**, *9*, 317 and references therein.
- (9) Granger, M. C.; Xu, J.; Witek, M.; Hupert, M.; Hanks, A.; Koppang, M. D.; Butler, J. E.; Lucazeau, G.; Mermoux, M.; Strojek, J. W.; Swain, G. M. *Anal. Chem.* **2000**, *72*, 3793 and references therein.
- (10) Backmann, P. K.; Wiechert, D. U. *Diamond Relat. Mater.* **1992**, *1*, 422.
- (11) Collins, A. T. *Diamond Relat. Mater.* **1992**, *1*, 457.
- (12) Zak, J. K.; Butler, J. E.; Swain, G. M. *Anal. Chem.* **2001**, *73*, 908.
- (13) Fayette, L.; Mermoux, M.; Marcus, B.; Rosman, N.; Abello, L.; Lucazeau, G. *J. Mater. Res.* **1997**, *12*, 2686.
- (14) Abstreiter, G.; Cardona, M.; Pinczuck, G. In *Light Scattering in Solids*; Cardona, M., Guntherodt, G., Eds.; Topics in Applied Physics, Vol. 54; Springer-Verlag: Berlin, 1984, p 6.
- (15) Locher, R.; Wagner, J.; Fuchs, F.; Maier, M.; Gonon, P.; Koidl, P. *Diamond Relat. Mater.* **1995**, *4*, 678.
- (16) Pruvost, F.; Deneuville, A. *Diamond Relat. Mater.* **2001**, *10*, 531.
- (17) Gonon, P.; Gheeraert, E.; Deneuville, A.; Abello, L.; Lucazeau, G. *J. Appl. Phys.* **1995**, *78*, 7059.
- (18) Ager, J. W., III; Walukiewicz, W.; McCluskey, M.; Plano, M. A.; Landstrass, M. I. *Appl. Phys. Lett.* **1995**, *66*, 616.
- (19) Pruvost, F.; Bustarret, E.; Deneuville, A. *Diamond Relat. Mater.* **2000**, *9*, 295.
- (20) Shiomi, H.; Kirillov, D.; Hagstrom, S. B. *Mater. Res. Soc. Symp. Proc.* **1993**, *283*, 897.
- (21) Wang, Y. G.; Li, H. D.; Lin, Z. D.; Feng, K. *Jpn. J. Appl. Phys.* **2000**, *39*, 2795.
- (22) Solin, S. A.; Ramdas, A. K. *Phys. Rev. B* **1970**, *1*, 1687.
- (23) Vogelgesang, R.; Alvarenga, A. D.; Kim, H.; Ramdas, A. K.; Rodriguez, S.; Grimsditch, M.; Anthony, T. R. *Phys. Rev. B* **1998**, *58*, 5408.
- (24) Haouni, A.; Mermoux, M.; Marcus, B.; Abello, L.; Lucazeau, G. *Diamond Relat. Mater.* **1999**, *8*, 657.
- (25) Bergman, L.; McClure, M. T.; Glass, J. T.; Nemanich, R. J. *J. Appl. Phys.* **1994**, *76*, 3020.
- (26) Robins, L. H.; Farabaugh, E. N.; Feldman, A. *J. Mater. Res.* **1990**, *5*, 2456.
- (27) Iakubovskii, K.; Adriaenssens, G. J. *Diamond Relat. Mater.* **2000**, *9*, 1017.
- (28) McCormick, T.; Jackson, W. E.; Nemanich, R. J. *J. Mater. Res.* **1997**, *12*, 253.
- (29) Iakubovskii, K.; Adriaenssens, G. J.; Vohra, Y. K. *J. Phys. C* **2000**, *12*, L519.
- (30) Iakubovskii, K.; Adriaenssens, G. J. *Phys. Rev. B* **2000**, *61*, 10174.
- (31) Iakubovskii, K.; Adriaenssens, G. J.; Nesladek, M. *J. Phys. C* **2000**, *12*, 189.
- (32) Iakubovskii, K.; Adriaenssens, G. J. *Diamond Relat. Mater.* **2000**, *9*, 1349.
- (33) Klein, P. B.; Crossfield, M. D.; Freitas, J. A.; Collins, A. T. *Phys. Rev. B* **1995**, *51*, 9634.
- (34) Ruan, J.; Kobashi, K.; Choyke, W. J. *Appl. Phys. Lett.* **1992**, *60*, 3138.
- (35) Hunn, J. D.; Withrow, S. P.; White, C.; Hembree, D. M., Jr. *Phys. Rev. B* **1995**, *52*, 8106.
- (36) Prawer, S.; Nugent, K. W.; Jamieson, D. N. *Diamond Relat. Mater.* **1998**, *7*, 106.
- (37) Orwa, J. O.; Nugent, K. W.; Jamieson, D. N.; Prawer, S. *Phys. Rev. B* **2000**, *62*, 5461.
- (38) Steeds, J. W.; Gilmore, A.; Bussmann, K. M.; Butler, J. E.; Koidl, P. *Diamond Relat. Mater.* **1999**, *8*, 996.
- (39) Anastassakis, E.; Pinczuck, A.; Burstein, E.; Pollak, F. H.; Cardona, M. *Solid State Commun.* **1970**, *8*, 133.
- (40) Grimsditch, M. H.; Anastassakis, E.; Cardona, M. *Phys. Rev. B* **1978**, *18*, 901.
- (41) Dannefaer, S.; Zhu, W.; Bretagnon, T.; Kerr, D. *Phys. Rev. B* **1996**, *53*, 1979.
- (42) Chandrasekhar, M.; Chandrasekhar, H. R.; Grimsditch, M.; Cardona, M. *Phys. Rev. B* **1980**, *22*, 4825.
- (43) Prawer, S.; Nugent, K. W.; Jamieson, D. N.; Orwa, J. O.; Burstill, L. A.; Peng, J. L. *Chem. Phys. Lett.* **2000**, *332*, 93.
- (44) Kim, H.; Vogelgesang, R.; Ramdas, A. K.; Rodriguez, S.; Grimsditch, M.; Anthony, T. R. *Phys. Rev. B* **1998**, *57*, 15315.
- (45) Wright, G. B.; Mooradian, A. *Phys. Rev. Lett.* **1967**, *18*, 608.